THE JOURNAL OF PHYSICAL CHEMISTRY B

Article

pubs.acs.org/JPCB

Structural and Rotational Dynamics of Carbon Dioxide in 1-Alkyl-3-methylimidazolium Bis(trifluoromethylsulfonyl)imide Ionic Liquids: The Effect of Chain Length

Chiara H. Giammanco, Steven A. Yamada, Patrick L. Kramer, Amr Tamimi, and Michael D. Fayer*

Department of Chemistry, Stanford University, Stanford, California 94305, United States

Supporting Information

ABSTRACT: Ionic liquids (ILs) have been proposed as possible carbon dioxide (CO_2) capture media; thus, it is useful to understand the dynamics of both the dissolved gas and its IL environment as well as how altering an IL affects these dynamics. With increasing alkyl chain length, it is well-established that ILs obtain a mesoscopic structural feature assigned to polar−apolar segregation, and the change in structure with chain length affects the dynamics. Here, the dynamics of CO_2 in a series of 1-alkyl-3-methylimidazolium bis(trifluoromethylsulfonyl)imide ILs, in which the alkyl group is ethyl, butyl, hexyl, or decyl, were investigated using ultrafast infrared spectroscopy by measuring the reorientation and spectral diffusion of carbon dioxide in the ILs. It was found that reorientation of the carbon dioxide occurs on three time scales, which correspond to two different time scales of restricted wobbling-in-a-cone motions and a long-time complete diffusive reorientation. Complete reorientation slows with increasing chain length but less than the increases in viscosity of the bulk liquids. Spectral diffusion, measured with two-dimensional IR spectroscopy, is caused by a combination of the liquids' structural fluctuations and reorientation of the CO_2. The data were analyzed using a recent theory that takes into account both contributions to spectral diffusion and extracts the structural spectral diffusion. Different components of the structural fluctuations have distinct dependences on the alkyl chain length. All of the dynamics are fast compared to the complete orientational randomization of the bulk ILs, as measured with optical heterodyne-detected optical Kerr effect measurements. The results indicate a hierarchy of constraint releases in the liquids that give rise to increasingly slower dynamics.

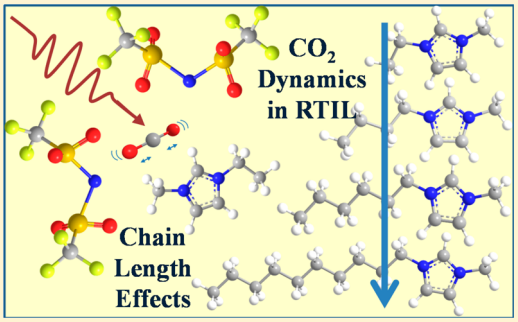

I. INTRODUCTION

Interest in technologies for the mitigation of carbon dioxide (CO_2) in air, either through a reduction in production or through capture of the gas before it enters the atmosphere, has increased significantly as the atmospheric levels of CO_2 are continuing to rise.[1,2] One of the largest anthropogenic sources of carbon dioxide is energy production through combustion of various fossil fuels. Although there has been much work performed on renewable sources, the current demand for energy requires fossil fuels in the energy mix for some time to come. Thus, the following question arises: how can the carbon dioxide released from burning fossil fuels be captured? There have been many systems proposed for the capture of carbon dioxide, including various solvents, amines, polymers, metal organic frameworks, and ionic liquids (ILs).[3,4] Several of these processes have already been employed in gas sweetening, that is, the removal of acid gases, including CO_2, before the gas is burned. Removal is achieved by having the gas of interest interact with an absorbing medium and then regenerating the medium and releasing the gas later for storage by either a pressure or temperature swing. Thus, it makes sense to consider the development of methods on the basis of these same processes, whereby carbon dioxide can be removed from the gas stream pre[5] or post[6] combustion. The target of the U.S. Department of Energy for the removal of carbon dioxide produced from power plant emissions is 90%, with no more than 20% increase in the cost of electricity.[7] This target cannot be achieved with current amine-based capture technology.[8] Thus, more-efficient removal and development of materials and conditions to optimize the process are required.

For postcombustion capture of CO_2 to be efficient, the capturing medium must be reusable several times. Thus, the capture material must be able to take out carbon dioxide from the waste gas stream selectively and in high yield, release the gas later (typically via a pressure or temperature swing) for collection, and then be recyclable. It is important that as little energy as possible is used to recover the CO_2 and that the capture medium continues working without degrading or evaporating over many cycles. Many molecular solvents employed to date can remove carbon dioxide effectively, but they require high pressures, which are inaccessible in postcombustion waste gas streams, and can suffer from evaporative losses and chemical decomposition.

Received: April 19, 2016
Revised: June 4, 2016
Published: June 5, 2016

DOI: 10.1021/acs.jpcb.6b03971
J. Phys. Chem. B 2016, 120, 6698−6711

Room temperature ILs (RTILs) are salts that remain molten at or below room temperature and may offer advantages for carbon capture. RTILs often have exceedingly low vapor pressures and therefore do not evaporate readily. Their chemical properties are also highly tunable, with constituent ions that are readily functionalized, and hence can be made task-specific.[9−12] Even without modification, several ILs, particularly those based on the imidazolium cation, show high solubility and selectivity for CO_2 at atmospheric pressures.[4,13−15] A few attempts have been made at functionalizing ILs for carbon capture through the addition of amine groups that can chemically bond with carbon dioxide.[16,17] However, the thermodynamic properties of these systems have not been thoroughly explored or optimized.[18,19] To find an optimal solvent, it is useful to understand what contributes to the carbon dioxide solvation structures and dynamics so that those properties can be enhanced for better capacities and capture kinetics.

The nanostructuring of RTILs has long been debated in the literature. Initial claims of long-range ordering have been adjusted to encompass ordering on shorter-length scales.[9] However, there is a consensus in the literature that as the alkyl chain lengthens an increased ordering or segregation of hydrophilic and hydrophobic regions over local domains is observed. Shorter chain lengths do not allow for the creation of a significant hydrophobic region, and no long-range ordering (other than charge−charge ordering) is realized. Longer chains enable polar and nonpolar regimes to segregate and to even form a bicontinuous phase when a sufficient length is reached.[9] Most notably, the increase in chain length causes a significant rise in viscosity, indicating that the average environment in solution has been substantially altered.

Several studies have focused on understanding the changing bulk physical properties in the 1-alkyl-3-methylimidazolium bis(trifluoromethylsulfonyl)imide series ($C_n$mimNTf$_2$).[20−23] There is some debate regarding the exact onset of aggregation of nonpolar groups sufficient to disrupt the structure and alter the IL properties. Sufficiently long alkyl tails lead to percolation of the nonpolar regions throughout the liquid and formation of a bicontinuous phase. An early X-ray scattering study puts long-range aggregation as occurring for chains longer than n = 3 carbons due to the appearance of a low-Q peak.[24] Although aggregation may begin here, molecular dynamics (MD) simulations indicate that the clusters do not begin to be sizable until at least n = 5.[25] A later analysis of X-ray and viscosity data showed a change in the properties at n = 6.[21,22] Thermodynamic quantities derived from the enthalpies and entropies of vaporization[21] as well as the heat capacity[20] were found to change for n > 6. This study focuses on how the increase in the alkyl chain, from n = 2 (EmimNTf$_2$), to n = 4 (BmimNTf$_2$), to n = 6 (HmimNTf$_2$), and then to n = 10 (DmimNTf$_2$) (see Figure 1), and concomitant changes in the structural ordering of the IL influences the dynamics of the dissolved CO_2 and that of the IL, using CO_2 as a probe.

1-Ethyl-3-methylimidazolium Bis(trifluoromethylsulfonyl)-imide (EmimNTf$_2$) is a particularly well-studied aprotic IL, which has a high CO_2 solubility,[13,26] low viscosity, and good thermal and electrochemical stabilities.[27,28] Previous studies have investigated the amount of carbon dioxide that various materials can hold as well as the rate of CO_2 translational diffusion through these materials.[14,29−37] Two recent studies have begun to look at the rotational and structural dynamics[38,39] of carbon dioxide in ILs. Both of these examined

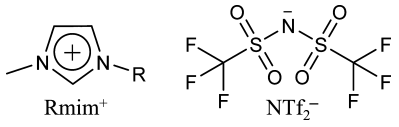

Figure 1. Structures of the ILs used: 1-alkyl-3-methylimidazolium bis(trifluoromethylsulfonyl)imide, where R = ethyl, butyl, hexyl, or decyl, abbreviated as EmimNTf$_2$, BmimNTf$_2$, HmimNTf$_2$, or DmimNTf$_2$ throughout the article.

the gas dissolved in ILs with a relatively short alkyl chain (EmimNTf$_2$ and the slightly larger BmimNTf$_2$). This article builds upon the previous studies by expanding the types of ILs studied and focuses on the effects of increasing alkyl chain length through the series. The reorientational dynamics are fairly straightforward to interpret, but the spectral diffusion data is more complex than that typically observed in two-dimensional (2D) IR spectroscopy. Recently, it was found that carbon dioxide in ILs undergoes the reorientation-induced spectral diffusion (RISD) phenomenon that has been described theoretically and observed in previous 2D IR studies.[39−41] Thus, analysis of spectral diffusion must take RISD into account to recover the true time scales of the structural spectral diffusion (SSD), that is, removing the effects of CO_2 reorientation on the spectral diffusion observable.

The organization of this article is as follows. Experimental procedures are discussed in Section II, including the following: A, sample preparation, and B, a brief description of the experimental ultrafast spectrometer. Results appear in Section III, broken down into the following parts: A, linear spectra, B, population relaxation of CO_2's stretch and bend, C, reorientation data and wobbling-in-a-cone analysis, and D, spectral diffusion analyzed using RISD theory with a second-order Stark effect coupling model. Concluding remarks follow in Section IV. Fitted curves for the analysis of isotropic population decays and the complete frequency−frequency correlation function (FFCF) parameters for the isotropic ensemble are given in the Supplemental Information.

II. EXPERIMENTAL PROCEDURES

II.A. Sample Preparation. The RTILs were purchased from IoLiTec Ionic Liquids Technologies Inc., dried for a week under vacuum and light heating to ∼60 °C, and stored in a nitrogen glove box. The water content of each was below 50 ppm, as determined by coulometric Karl Fischer titration. $^{13}CO_2$ (<99% isotopic purity) was purchased from Icon Isotopes and used without further purification. Isotopically labeled carbon dioxide was bubbled through the RTIL in an evacuated vial, with care taken to exclude atmospheric moisture. The IL−CO_2 mixture was sandwiched between 3 mm CaF_2 windows, separated by a Teflon spacer. The sample cells were assembled in a dry atmosphere to prevent water uptake by the IL. Linear IR spectra were recorded with a Thermo Scientific Nicolet 6700 Fourier transform infrared (FTIR) spectrometer. Background spectra of the IL without the addition of $^{13}CO_2$ were recorded under identical conditions and subtracted from those of the IL with carbon dioxide to give the contribution from $^{13}CO_2$ alone. The carbon dioxide concentration was kept sufficiently low, such that vibrational excitation transfer between adjacent molecules was statistically unlikely to occur. Using the extinction coefficient of carbon dioxide in water[42] and aluminosilicate glasses,[43] the concentration was

DOI: 10.1021/acs.jpcb.6b03971
J. Phys. Chem. B 2016, 120, 6698−6711

estimated to be around 2000 ion pairs per carbon dioxide from the background-subtracted FTIR spectrum (Section III.A).

II.B. Ultrafast Infrared Techniques. Data were acquired on two different experimental 2D IR setups, for which the layout and procedures have been described in detail previously.[44,45] Polarization-selective 2D IR spectra and IR pump−probe measurements were recorded. Both apparatuses shared the same general layout. Briefly, a Ti:Sapphire oscillator/regenerative amplifier system pumped an optical parametric amplifier (OPA) based on a beta barium borate crystal at a 1 kHz rep rate. The output of the OPA was difference-frequency mixed in a $AgGaS_2$ crystal to create mid-IR pulses. The mid-IR beams propagated through an enclosure purged to minimize atmospheric absorption, with air scrubbed of water and carbon dioxide. Some carbon dioxide remained despite the purge, but the isotopic labeling shifted the probe absorption away from the $^{12}CO_2$ wavelength so that the data were not distorted by atmospheric $^{12}CO_2$ absorption.

The IR light was split into two beams, a stronger pump and weaker probe, for both the pump−probe and vibrational echo measurements. To collect pump−probe data, the pump beam polarization was rotated to 45° relative to the horizontally polarized probe using a half-wave plate and polarizer and was mechanically chopped at half the laser repetition rate. The pump and probe beams were focused and crossed in an approximately 100 μm diameter spot at the sample. The relative pump−probe delay was set precisely using a mechanical delay stage. After traversing the sample, the probe polarization was resolved either parallel or perpendicular to that of the pump beam by a computer-controlled rotatable polarizer. The probe polarization was projected back to horizontal using a polarizer following the measurement but before frequency dispersal and detection. The pump−probe signal experiments were dispersed by a spectrograph with a 300 line/mm grating and detected on a 32 pixel liquid-nitrogen-cooled mercury−cadmium−telluride array.

For vibrational echo experiments, three IR pulses of the desired polarizations impinge on the sample and stimulate the emission of the vibrational echo in the phase-matched direction. To obtain phase information, the echo was heterodyned with a local oscillator (LO). Because the first two pulses in the vibrational echo pulse sequence are collinear, the echo is emitted collinearly with the third excitation pulse, which also serves as the LO. The time between pulses 1 and 2 is scanned, causing the vibrational echo phase to evolve in time relative to the stationary LO pulse. The resulting temporal interferogram is frequency-resolved and detected on a 32-element liquid-nitrogen-cooled mercury−cadmium−telluride array, which provides the vertical axis, ω_m, of the 2D IR spectra. At each ω_m, the interferogram is numerically Fourier transformed to give the horizontal axis, ω_τ, of the 2D IR spectra.

The two setups employed differed in the bandwidth supported (and thus minimum pulse duration) and pixel width of the detecting array. The first system[44] was used for pump−probe measurements. It afforded greater time resolution, as it had shorter pulses (~65 fs). This system was modified with a diverging lens (f = −7.5 cm) after the spectrograph (located slightly before the exit focal plane) to further spread out the dispersed wavelengths spatially. This setup enabled the array detector, with its relatively wide pixels (0.5 mm width), to better sample the resolution supplied by the spectrograph. Spectral data were retrieved every 0.6 cm^{-1}.

The second system[45] was employed in the acquisition of the 2D IR vibrational echo signal, and it was configured in a pump−probe geometry, with a germanium acousto-optic mid-infrared pulse shaper. Three incident pulses, the first two of which are generated collinearly by the pulse shaper, stimulated the emission of the vibrational echo in the phase-matched direction, which is collinear with the third (probe) pulse. The probe also serves as the LO for optical heterodyne detection of the echo signal. Although this system did not support as great an IR bandwidth as the first (and thus did not have as short a time resolution), there was significantly more power at the vibrational probe absorption wavelengths, and it was outfitted with an array detector with narrower pixels (0.1 mm). The narrow pixels enabled sampling the spatially dispersed spectral data with greater resolution. A width equivalent to several pixels separates the thin detector elements. To collect the frequencies lost between pixels, the monochromator center was shifted by half the pixel-to-pixel frequency spacing. The two blocks of data, with 32 detection frequencies each, were interlaced to yield one complete data set at 64 frequencies. The pulse shaper enables phase cycling and collection of echo interferograms in the partially rotating frame for scatter removal and rapid data acquisition. The pulse shaper additionally allows 2D IR data to be worked up without the need for phase corrections in postprocessing[46,47] because the echo signal is self-heterodyned by collinear pulse 3, which serves as the LO. This method results in no uncertainty in the relative timing of pulses that define coherence periods during which there is rapid phase evolution.[45,48,49]

III. RESULTS AND DISCUSSION

III.A. Linear IR Spectrum. Carbon dioxide has a strongly absorbing asymmetric stretch, which is easily monitored with IR spectroscopy. The peak of unlabeled carbon dioxide ($^{12}CO_2$) shifts from 2350 cm^{-1} in the gas phase to 2342 cm^{-1} when solvated by RTIL $EmimNTf_2$. The vibrational probe used was ^{13}C-labeled CO_2 to avoid the interference of atmospheric carbon dioxide (predominantly $^{12}CO_2$) with the signal. The asymmetric stretch of the isotopically labeled $^{13}CO_2$ absorbs at ~2276 cm^{-1} in the IL, with the wavelength dependent on the RTIL chain length (see Figure 2). Although unlabeled carbon dioxide is a good probe in itself,[38,50] we have chosen to use an isotopically labeled species to limit the effects of atmospheric carbon dioxide interference with the measurement and distortion of the results.

Carbon dioxide dissolves quite readily in 1-alkyl-3-methylimidazolium bis(trifluoromethylsulfonyl)imide ILs.[13,26] Imidazolium-based ILs typically can solubilize large quantities of the gas, comparable to or better than that by other common cations in terms of mole fraction dissolved.[4,14,32,51] However, the anion is more important for the solubility.[26,32] Experiments and MD simulations show a greater affinity for and stronger organization of the CO_2 molecules around the anion.[26] The identity of anion, and to a lesser extent the cation, can cause the center of the linear IR absorption spectrum of CO_2 to shift and broaden. The partial charges on the isolated carbon dioxide molecule are rather large, with the carbon having a charge of +0.70 and each oxygen having a charge of −0.35;[52] thus, it associates quite readily with the polar groups of the IL. There is very little volume expansion when the gas is added to the IL.[53] The anion radial distribution function changes little upon the addition of CO_2,[26] suggesting that the IL structure remains relatively unperturbed by the addition of small amounts of carbon

DOI: 10.1021/acs.jpcb.6b03971
J. Phys. Chem. B 2016, 120, 6698−6711

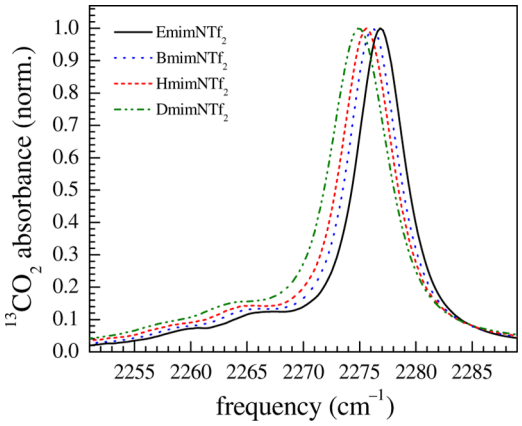

Figure 2. Background-subtracted FTIR spectra of the asymmetric stretch of $^{13}CO_2$ in $EmimNTf_2$ (black), $BmimNTf_2$ (blue), $HmimNTf_2$ (red), and $DmimNTf_2$ (green). Note that there is a shoulder to the red side of each main band, which is caused by a hot band absorption of the asymmetric stretch when the bend is already thermally excited.[54] It appears at a frequency lower than the main asymmetric stretch absorption by the combination band shift. A small additional peak shows up even farther than the red that is caused by small amounts of $^{18}O^{13}CO$.

dioxide, in contrast to that of more typical solvents. To a first approximation, carbon dioxide occupies the spaces in the RTIL that would otherwise be vacant.[53]

To the red (low-frequency) side of the main absorption, there is a noticeable shoulder, both with labeled and unlabeled CO_2 and in all of the RTILs studied (Figure 2). It has been shown[38,54] that this shoulder is a hot band, the result of the thermally populated bend coupling to the asymmetric stretch; the absorption shows up red-shifted by the combination band shift. Whereas the hot band does not contribute directly to the observed signal because of its red shift and low amplitude, its coupling to the fundamental transition does affect the analysis of isotropic population decay data. This topic has been addressed in a previous investigation.[54] The observation of structural dynamics through spectral diffusion within the fundamental band and anisotropic reorientation dynamics is unaffected by the small isotropic population effects.[55] A very small peak further to the red is attributed to molecules that contain an ^{18}O instead of two ^{16}Os. This is reasonable as the $^{13}CO_2$ gas is slightly enriched in ^{18}O, according to the manufacturer's specifications. This peak has a low amplitude, and it is shifted sufficiently from the main peak; hence it does not interfere with the experiments.

The absorption band (Figure 2) of CO_2 in $EmimNTf_2$ is the narrowest, with a 4.9 cm^{-1} full width at half-maximum (FWHM). As the chain length increases, the peak shifts toward the red and broadens to 5.9 cm^{-1} FWHM in $DmimNTf_2$. A summary of the peak positions and widths is shown in Table 1. These are all somewhat narrower than the ~7 cm^{-1} FWHM absorption spectrum of CO_2 in water,[50] but peak narrowing in an IL versus that in other solvents is typically observed.[55−57] The narrowness of the band suggests either that the vibrational frequency does not change greatly as the carbon dioxide experiences different environments in the IL or that the dissolved gas molecules are found in a limited range of configurations.

The small changes in width and peak shift suggest that there is a greater range of environments available to the carbon

Table 1. Linear Absorption Peak Centers and Widths for the CO_2 Asymmetric Stretch in Molecular and IL Solvents

solvent	center (cm^{-1})	FWHM (cm^{-1})
water	2277.9 ± 0.1	7.3 ± 0.1
$EmimNTf_2$	2276.9 ± 0.1	4.9 ± 0.1
$BmimNTf_2$	2276.2 ± 0.1	5.2 ± 0.1
$HmimNTf_2$	2275.7 ± 0.1	5.4 ± 0.1
$DmimNTf_2$	2275.0 ± 0.1	5.9 ± 0.1
hexadecane	2270.3 ± 0.1	7.7 ± 0.1

dioxide as the chain length increases. In $DmimNTf_2$, there are definite polar and nonpolar regions that are not present in $EmimNTf_2$.[25] One could argue that the carbon dioxide is partitioning between the two regions and the signals from the separate populations overlap to give the broader absorption. This seems unlikely, however, as CO_2 is known to interact predominantly with anions, as discussed above. In addition, fitting the absorption curves shown in Figure 2 from the blue side to two-thirds of the way down the red side (to avoid the hot band on the red shoulder) yields perfect fits to a Voigt function. The quality of the Voigt fits demonstrates that the lines are symmetrical and that there is no evidence of broadening around the peaks of the lines. Thus, these fits virtually rule out two overlapping slightly displaced absorption lines.

To understand better what carbon dioxide asymmetric stretch absorption in a completely nonpolar environment looks like, we took an FTIR of CO_2 bubbled through *n*-hexadecane (see Figure 3, red dot-dashed curve). In Figure 3, the results of fits to the main portions of the spectra are shown to eliminate the shoulders on the red sides of the lines. In *n*-hexadecane, the center is shifted to a significantly lower frequency, 2270.3 cm^{-1}. A scaled combination of the CO_2 spectrum in hexadecane with the spectrum in $EmimNTf_2$

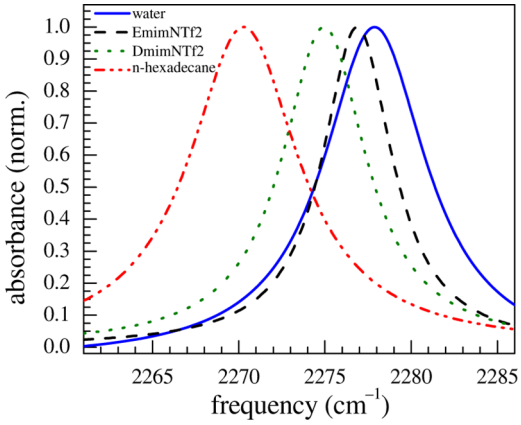

Figure 3. Fits to the FTIR spectra of the main peak of $^{13}CO_2$ in water (blue), $EmimNTf_2$ (black), $DmimNTf_2$ (green), and *n*-hexadecane (red). Fits were used so that the spectra can be compared without the hot bands. The curves are normalized. Note that the spectrum of carbon dioxide associated with nonpolar hexadecane is substantially red-shifted from that for the more polar solvents. No combination of the Emim and hexadecane spectra will reproduce the $DmimNTf_2$ spectrum, indicating that carbon dioxide does not readily dissolve in the nonpolar regions of the IL. Moreover, the $DmimNTf_2$ spectrum is then not the sum of two populations but rather the result of different environments present in solution felt by a single CO_2 ensemble located in the polar region.

DOI: 10.1021/acs.jpcb.6b03971
J. Phys. Chem. B 2016, 120, 6698−6711

cannot create the peak shift seen from $EmimNTf_2$ to $DmimNTf_2$ and does not result in a symmetrical spectrum. For comparison, Voigt fits to the main peaks of the background-subtracted FTIR spectra of carbon dioxide in water (blue solid curve), $EmimNTf_2$ (black dashed curve), and $DmimNTf_2$ (green dotted curve) are also shown in Figure 3. From Figure 3, it can also be seen that the peak center of the absorption of CO_2 in the ILs is closer to that of the spectrum in water than that in hexadecane. It may be that the polarity of the solvent influences the peak position, which would suggest that the carbon dioxide in longer chain lengths senses the overall decrease in polarity. Note also that the peaks in the non-ILs are much broader than those in the ILs, suggesting that there is a smaller variation in environments in the ILs. From the linear spectra, we can conclude that the increasing chain length of the cation and resulting change in the structure of the IL affect the dissolved carbon dioxide molecules.

We conclude then that there is a single population present in $DmimNTf_2$, the carbon dioxide does not go into the nonpolar regions created by lengthening the alkyl tail, and that the increased structuring of the IL instead causes the CO_2 to access a broader range of local environments. These results are consistent with the MD simulations of Shimizu et al., who found that the average number of contact neighbors for ions in the polar region changes from 5 to 4 as the chain length increases from 2 to 10.[25] As the structure of the polar region changes, different environments are presented to the carbon dioxide, and its spectrum is correspondingly affected. Further evidence corroborating these conclusions is presented below.

III.B. Population Relaxation. To determine both the population relaxation (vibrational lifetime) and anisotropy (reorientation dynamics), polarization-selective pump−probe experiments were performed. The polarization of the pump pulse is set at 45° relative to the horizontal probe, and the polarizations of the probe signals parallel, $S_{\parallel}(t)$, and perpendicular, $S_{\perp}(t)$, to the pump are then resolved. These signals can be expressed in terms of population relaxation $P(t)$ and the second Legendre polynomial orientational correlation function, $C_2(t)$

$$S_{\parallel}(t) = P(t)[1 + 0.8C_2(t)] \quad (1)$$

$$S_{\perp}(t) = P(t)[1 - 0.4C_2(t)] \quad (2)$$

The normalized population relaxation is given by

$$P(t) = \frac{1}{3}[S_{\parallel}(t) + 2S_{\perp}(t)] \quad (3)$$

At early times, an instantaneous nonresonant signal, which tracks the pulse durations, interferes with the signal from the resonant vibrations. Thus, only the data after 300 fs is used. Typically, the vibrational relaxation deposits a small amount of heat into the sample, which can result in a constant isotropic signal at long time due to a temperature-dependent spectral shift.[58,59] However, in this IL system, the heating is very small. In an approximation to the heat removal technique, data were taken out to long time (500 ps), the long-time offset was fit, and the obtained constant value was subtracted from the data. However, this amount was so small that it was insignificant, and removing it from the data did not change the shape of the curves, and the fit results were the same within experimental error.

The medium surrounding a solvated-molecule influences the coupling and density of states of the modes that can receive energy from the relaxing initially excited vibration.[60] Thus, the vibrational population relaxation time scale depends on the environment in which a molecule is located. If there are two distinct environments for the probe in solution, these environments will give rise to different lifetimes, unless, by coincidence, the sums of the relaxation rates for all pathways in the different environments are equal. Some processes can also produce nonexponential decays of the population relaxation. If the band is pumped nonuniformly or the transition dipole varies across the band (non-Condon effects), the initial population in the excited state will not match the equilibrium distribution. Spectral diffusion will cause additional decays at some wavelengths and growths at others.[55] Population transfer can also cause growths or decays if the system is not initially at equilibrium. As described in detail in previous work,[54] we analyze these short-time nonexponential decays using a model based on population transfer between the main peak and combination band. The transition dipole moments of these two populations are not equal and thus they are pumped to a nonequilibrium state, from which they then equilibrate producing a small growth contribution to the population of the main band at short times.

The ratio of molecules that are expected to have thermally populated bends to no bend excited is calculated using the Bose−Einstein distribution. We take the bend frequency to be 641 cm^{-1}, as was found for $EmimNTf_2$ in the previous analysis. As the peak of the carbon dioxide absorption shifts from $EmimNTf_2$ to $DmimNTf_2$ by 2 cm^{-1}, the bend frequency might shift as well. However, a change in the bend frequency of as much as 5 cm^{-1} is not sufficient to give different fits; thus, this effect is disregarded. The transition dipoles of the asymmetric stretches, with the bend excited and in the ground state, can be determined by fitting the linear spectra. Fits of the areas of the main band (no bend excited, A_{nb}) and hot band (with the excited bend, A_b) were performed, and the ratios appear in the first column of Table 2. Because of the isotopic peak from $^{18}O^{13}CO$, good fits require that all three overlapping peaks be fit at once. Whereas the main band is well-defined, overlap with the $^{18}O^{13}CO$ peak leads to significant error in the area of the hot band and thus in the ratio. However, even with the error, all four RTILs have about the same ratio of peak areas and thus the same ratio of transition dipoles. The coupling of the asymmetric stretch to the bend results in a band with a stronger transition when the bend is excited than that when it is not, and this relationship is not substantially altered by the identity of the solvating liquid. The overpumped band then relaxes toward the equilibrium population, which results in an early-time growth in the population relaxation of the initially under-pumped fundamental transition. Using this dipole ratio information, a kinetic model (derived previously[54]) can be fit to the data to give the lifetime of asymmetric stretch τ_1 and bend relaxation time τ_b. Data and fits to the peak wavelength in

Table 2. Population Relaxation Fit Parameters for the CO_2 Asymmetric Stretch and Bend

IL	A_{nb}/A_b	τ_1	τ_b
$EmimNTf_2$	8.2 ± 0.6	64 ± 2	13 ± 2
$BmimNTf_2$	8.4 ± 0.6	64 ± 2	18 ± 2
$HmimNTf_2$	7.9 ± 0.6	63 ± 2	18 ± 2
$DmimNTf_2$	7.8 ± 0.6	62 ± 2	18 ± 2

DOI: 10.1021/acs.jpcb.6b03971
J. Phys. Chem. B 2016, 120, 6698−6711

each solvent are available in the Supporting Information, Figure S1. Table 2 contains the relaxation times derived from the fits.

The lifetime of the asymmetric stretch varies slightly with an increase in chain length from 64 ± 2 to 62 ± 2 ps, although these are within the error bars of each other. The presence of a single lifetime decay is further evidence that there is a single population of absorbers in solutions. Vibrational lifetimes are very sensitive to the medium in which the vibration is embedded. The lifetime of the stretch depends on the very local environment around the probe that gives rise to the accepting bath modes to which the vibrational energy will be transferred. The lack of a strong dependence of the lifetime on chain length does not necessarily mean that the environments are identical but rather that the presence of nonpolar domains does not significantly change the density of states and couplings of the intramolecular and intermolecular modes of the surrounding RTIL to the carbon dioxide asymmetric stretch.

The bend lifetime, however, does change. In the RTILs with a longer chain length, the bend lifetime increases to 18 ± 2 ps from 13 ± 2 ps in $EmimNTf_2$. The difference suggests that the presence of the larger nonpolar regions and their influence on the polar regions changes the environment around the CO_2 sufficiently to produce weaker coupling between the bath modes and the bend, leading to a longer bend lifetime. These results indicate that there is a change in the ionic region structure from Emim to Bmim, but the change is less-pronounced in going from Bmim to RTILs with even longer chains. More evidence for this type of chain length progression is presented in the subsequent sections.

III.C. Anisotropy. The orientational relaxation can be addressed from the same pump−probe data used to obtain the vibrational lifetimes discussed above. The anisotropy is equal to the transition dipole orientational correlation function (the second Legendre polynomial correlation function, $C_2(t) = \langle P_2(\hat{\mu}(t)\cdot\hat{\mu}(0))\rangle$) scaled by 0.4. It has the form

$$r(t) = \frac{S_{\parallel}(t) - S_{\perp}(t)}{S_{\parallel}(t) + 2S_{\perp}(t)} = 0.4C_2(t) \quad (4)$$

Fits of the curves do not achieve 0.4 (perfect correlation) when extrapolated back to time zero. The apparent reduction from 0.4 at $t = 0$ is caused by fast inertial motion that is complete within the overlapped pulse durations at short time and cannot be resolved. By analyzing the difference between 0.4 and the extrapolated $t = 0$ value, the magnitude of the inertial reorientation can be quantified.

After the initial inertial drop, the curves decay in a nonexponential manner and fit well to triexponential decays (see Figure 4 and the inset). Because there is only one population, as seen from the linear spectra and lifetime measurements, these are interpreted as the time scales for constrained reorientation in successively larger cones and then on the longest time scale, complete rotational randomization. The wobbling-in-a-cone model is used to analyze the short-time restricted orientational relaxation,[61−64] whereas complete randomization is described as free diffusion. The anisotropy decay curves are fit simultaneously for the various detection wavelengths across the band, allowing the amplitudes of each relaxation component to vary while sharing the time constants. As can be seen for $DmimNTf_2$ data in Figure 4, the fits reproduce the data exceedingly well. The fits to the other RTILs (not shown) are similar in form and quality. The inset of Figure 4 is a zoomed-in view of the curves at early time to show

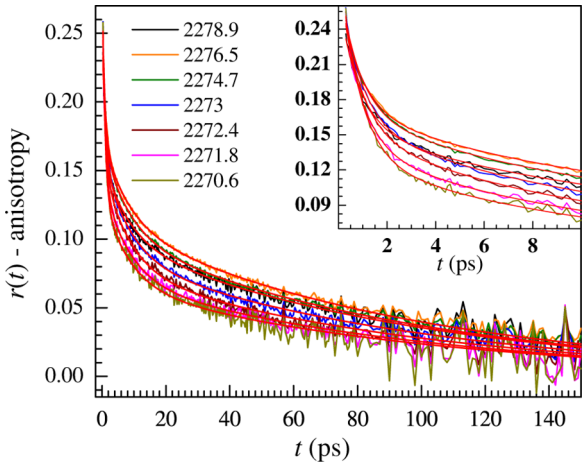

Figure 4. Representative anisotropy decays for $DmimNTf_2$ are plotted for selected wavelengths (cm^{-1}) across the band. Fits to the curves are shown in red. Note that the data fit very well to a triexponential form across all wavelengths, with the time constants shared but the amplitudes allowed to vary. The variation in the measured anisotropy with wavelength is attributed to different wobbling motions across the band. The inset shows the early-time data more clearly. The anisotropy curves in the other ILs are of similar shape and quality, with fits that agree equally well with those of the data.

the quality of the fit. Allowing the long-time constant to vary did not improve the fit and made the wavelengths with lower signal (i.e., on the red and blue edges of the band) more susceptible to noise. The time constants from the fits are given in Table 3. τ_{c1} is the time constant for sampling cone 1, τ_{c2} is

Table 3. Time Scales of Reorientation from the Pump−Probe Anisotropy Fits, Wobbling-in-a-Cone Analysis, and Hydrodynamic Predictions

IL	τ_{c1} (ps)	τ_{c2} (ps)	τ_m (ps)	τ_m^{slip} (ps)
$EmimNTf_2$	0.91 ± 0.03	8.3 ± 0.1	54 ± 1	45
$BmimNTf_2$	0.81 ± 0.03	7.9 ± 0.2	67 ± 2	66
$HmimNTf_2$	0.81 ± 0.03	8.2 ± 0.3	74 ± 2	91
$DmimNTf_2$	0.81 ± 0.03	8.8 ± 0.6	96 ± 4	158

the time constant for sampling cone 2, and τ_m is the time constant for the final diffusive complete orientational relaxation. Each cone decay reflects a decay to a plateau that is determined by the cone angle, which is then followed by the decay from the plateau by the next slower process. The decay constants, τ_{c1} and τ_{c2}, are obtained from the triexponential fit after the small contribution from the next slower decay has been removed. τ_m is the slowest decay constant in the triexponential fit.

The wobbling-in-a-cone half-angles for each of the three restricted rotation processes (the inertial cone and two diffusive cones) are obtained from the triexponential fits to the data using the standard approach.[55,61,63,65] The averaged cone angles across the band are given in Table 4. From the time constants in Table 3 and cone half-angles, the diffusion constants for each cone can be obtained.[65] Note that aside from the difference in the inertial cone between $EmimNTf_2$ and the RTILs with a longer chain length, the cones are very similar in size (half-angle); the angles are equal within experimental error. The total cone half-angle is ∼51° for all of the RTILs, after which the carbon dioxide undergoes the long-time complete orientational randomization. Even though the time constant for this slowest

DOI: 10.1021/acs.jpcb.6b03971
J. Phys. Chem. B 2016, 120, 6698−6711

Table 4. Cone Half-Angles in Degrees for Restricted Orientational Relaxation, Averaged Across the Vibrational Band

IL	inertial cone	1st wobbling cone	2nd wobbling cone	total cone
$EmimNTf_2$	20 ± 2	32 ± 2	35 ± 2	50 ± 2
$BmimNTf_2$	26 ± 2	32 ± 2	33 ± 2	51 ± 2
$HmimNTf_2$	26 ± 1	33 ± 2	32 ± 3	51 ± 2
$DmimNTf_2$	27 ± 1	33 ± 2	33 ± 3	52 ± 2

motion increases with chain length, the faster wobbling motions occur with similar amplitudes as well as on similar time scales (Table 3). This suggests that the motions of the carbon dioxide are gated by the IL. To sample the orientational space, the probe molecule must wait for the IL surroundings to move. With the exception of the jump in the first cone time constant in going from Emim to Bmim, all of the wobbling time constants do not show a trend with chain length within experimental error (Table 3).

Assessing the wavelength dependence of the cone angles yields more insight into the differences between the RTILs. Figure 5 plots the different cone angles experienced across the band. Note that the frequency (horizontal) axis is displayed as detuning in wavenumbers (cm^{-1}) from the absorption peak center in the corresponding RTIL. This enables a better comparison of the different cones because the peak red-shifts with chain length (see Figure 2). Figure 5A shows the inertial cone. The inertial cone is significantly larger for RTILs with a longer chain length (blue, red, and green) than that for short-chain $EmimNTf_2$ (black). For the most part, the inertial cone angle is not wavelength-dependent, although $BmimNTf_2$ (blue) appears to show a weak trend toward a larger cone angle with higher frequency. For $HmimNTf_2$ and $DmimNTf_2$, there may also be the same trend, but if so, it is almost within the error bars. The major difference is between $EmimNTf_2$ and the other three RTILs.

Figure 5B shows the first wobbling cone. This cone amplitude and time constant are highly conserved among different RTILs. Note that the cone angle is dependent on frequency and reaches a minimum at ~1 cm^{-1} blue of peak center for all of the chain lengths. This identical trend for the four liquids suggests that the amplitude of this motion results from very similar mechanisms in all of the RTILs. Likely, this would then be determined by an interaction with the anion, which is unchanged in the four RTILs. There may also be interactions with the cation head group but in a manner that is independent of the chain lengths. Either way, it suggests that there is a geometric constraint on the carbon dioxide molecule such that its most common environments in the liquid (and thus near the center of the absorption band) are also the most angularly restricted.

The simplest model to explain how the transition frequency ω of the carbon dioxide varies in response to environmental fluctuations to give the observed band is the Stark effect, the coupling of the frequency to the local electric field experienced by the probe molecule, which results from all charges in the medium. (Below, it will be shown that the Stark effect is necessary to explain the 2D IR spectral diffusion data.) Expanded up to second order in the field, the frequency is given by

$$\omega = \omega_0 - \Delta\vec{\mu}\cdot\vec{E} - \frac{1}{2}\vec{E}\cdot\Delta\alpha\cdot\vec{E} \quad (5)$$

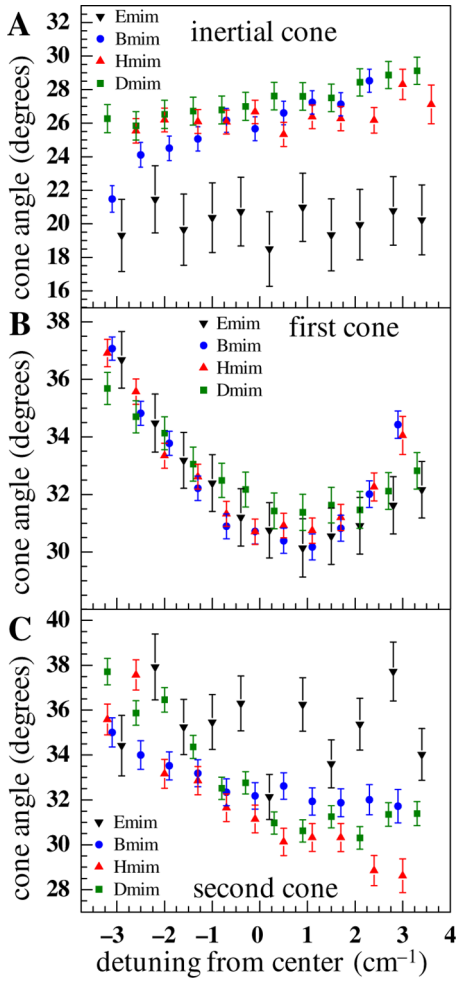

Figure 5. Results of the wobbling-in-a-cone analysis of $^{13}CO_2$ in $EmimNTf_2$ (black), $BmimNTf_2$ (blue), $HmimNTf_2$ (red), and $DmimNTf_2$ (green), plotted as cone half-angle vs the distance in frequency from the band center. The inertial cone (A) shows little variation with wavelength for Emim but a slight change for the longer alkyl chain ILs. The first wobbling cone (B) is very strongly correlated with wavelength, in a manner that is highly conserved in all four RTILs. The second wobbling cone (C) has no wavelength dependence in Emim but varies somewhat across the band for the longer chains.

where ω_0 is the natural oscillator frequency in the absence of electric fields, $\vec{E}$ is the net electric field vector at the position of the molecule, $\Delta\vec{\mu}$ is the dipole moment difference between the first excited state ($n = 1$) and ground state ($n = 0$), and $\Delta\alpha$ is the difference in polarizability tensor between the 1 and 0 states.[66−68] Note that for carbon dioxide, which does not have a permanent dipole, $\Delta\vec{\mu} = 0$. For now, assume that $\Delta\alpha$ is positive, which is relatively common.[69] The discussion is entirely analogous if $\Delta\alpha$ were negative, only with red and blue frequencies reversed. We would expect that increasing alignment with the field would cause a red shift and decreasing alignment (toward being oriented at 90° to the field) would cause a blue shift from the average center frequency. The first cone angle wavelength dependence indicates that configurations that give rise to either alignment with or perpendicular to the field give rise to more angular freedom, that is, the ion packing around the CO_2 permits an increase in the range of angles that can be sampled. Both the electric fields and confining potential result from the arrangement of IL cations and anions around the CO_2 solute, so it is reasonable that

DOI: 10.1021/acs.jpcb.6b03971
J. Phys. Chem. B 2016, 120, 6698−6711

similar confining potentials can result in similar electric field vectors (and therefore vibrational frequencies). The bulky ions prevent the CO_2 solute from undergoing free diffusion. Rather, on a short time scale compared to that of constraint release, the pockets available to CO_2 in the dense IL matrix limit the angular range, and that range depends to some extent on the details of the local configurations of ions.

Figure 5C shows the wavelength dependence of the second wobbling cone. Whereas short-chain $EmimNTf_2$ (black) displays no wavelength dependence within the error bars, RTILs with a longer chain have a definite downward trend in cone half-angle as the frequency increases. This is opposite to the trend seen by hydrogen bonding solutes in $EmimNTf_2$.[55] The blue (higher frequency) side of the line of a hydrogen bond donating probe molecule is made up of absorbers with weaker hydrogen bonds that allow for larger angular excursions during wobbling. The carbon dioxide is not restricted by hydrogen bonds; thus, the allowed angular deviation is more a reflection of the restrictions present for particular ion solvation shell configurations. These particular configurations give rise to varying carbon dioxide vibrational frequencies modeled as arising from the electric field, as discussed above. Whereas in $EmimNTf_2$ the different configurations have about the same angular restriction on the second cone wobbling time scale, in ILs with a longer chain length, this is not the case. The presence of aggregation of the nonpolar alkyl chains impacts the structural configurations available to the polar regions in which CO_2 is solvated. Configurations leading to CO_2 molecules on the high-frequency side of the spectra are more angularly constrained. Ions must undergo some structural rearrangement following the angular sampling of the first wobbling period (Figure 5B) to allow an increase in the restricted angular motion in the second wobbling period (Figure 5C). The longer alkyl chains reduce the cone angle that can be sampled by the solute compared to that by CO_2 in $EmimNTf_2$, in which the polar region encompasses the entire liquid.

Let us then summarize what the cone angle analysis says about the differences in the RTILs, as reflected in the CO_2 dynamics. The inertial cone data (Figure 5A) and second cone (Figure 5C) show that Emim has structural constraints on angular sampling that are different from those of the three RTILs with longer chains. The positive charge on the cation is delocalized and extends to the first two carbons of an alkyl chain. $EmimNTf_2$ does not have a nonpolar region, whereas the other three liquids do. Apparently, this difference affects the structure in the ionic regions that gives rise to the angular constraints. It is interesting that within error there is no difference between Emim and the other three RTILs in the first wobbling cone. The lack of a difference between Emim and the other three RTILs for the first cone angles indicates that the presence of the alkyl chains impacts some types of ion configurations but not others, and the effect of the presence of nonpolar regions depends on the time scales of the observations.

Whereas the wobbling cones suggest similarities among the different RTILs, the long-time constant for reorientation in the RTILs, τ_m, slows significantly with increasing chain length. τ_m is equal to $1/(6D_m)$, where D_m is the diffusion constant for this final rotational randomization process, which occurs by free diffusion. As the chain length increases, so does the viscosity. The viscosities were measured to be 38.0 cP ($EmimNTf_2$), 56.1 cP ($BmimNTf_2$), 77.5 cP ($HmimNTf_2$), and 134.4 cP ($DmimNTf_2$) at 23.2 °C, the temperature at which the experiments were conducted. An increase in viscosity should lead to a decrease in the rate of orientational diffusion. The measured time constant for orientational randomization of the probe can be compared to that of predictions of rotational diffusion in the hydrodynamic limit, using a modified Debye−Stokes−Einstein equation. If diffusive motion is well-described by hydrodynamics, we can relate the orientational relaxation time to properties of the system by[70]

$$\tau_m = \frac{fV_{eff}\eta}{k_B T} \tag{6}$$

where T is the absolute temperature, η is the viscosity, k_B is Boltzmann's constant, and V_{eff} is the effective molecular volume. The shape factor is $f = 1$ for stick boundary conditions and $f(\rho)$ for slip conditions, where ρ is the axial ratio of the molecular ellipsoid. Stick boundary conditions lead to much slower time constants than those observed experimentally. Stick boundary conditions apply when the friction opposing reorientation is the adhesion of smaller solvent molecules to a large solute under study, which clearly does not reflect the present situation; the small carbon dioxide molecule is solubilized in the RTILs, which are composed of ions that are much larger than CO_2. Slip boundary conditions apply when the friction opposing reorientation arises from the presence of solvent in the swept volume of the probe. Therefore, slip boundary conditions are a reasonable model for CO_2's reorientational friction. The ρ dependence of f with the slip boundary conditions has been calculated by Youngren et al. and Hu et al.[71−73] We estimate the dimensions of the carbon dioxide molecule using the known bond length, 116 pm,[74] and van der Waals radii of carbon and oxygen. The effective volume is then $V_{eff} = 22.4$ Å^3, $\rho = 0.58$, and $f = f(\rho) = 0.215$ for a prolate spheroid. Calculated τ_m^{slip} values appear next to measured τ_m values in Table 3.

Comparing measured τ_m and calculated τ_m^{slip} for the four RTILs, the values are reasonably close. However, even though reorientation slows down as the chain length increases, it does so less than the increase in viscosity would dictate. The predicted hydrodynamic times go from faster than the measured time for Emim to substantially slower than the measured time for Dmim. The predicted change from the hydrodynamics calculation shows that the reorientation should slow by ∼3.5 in going from Emim to Dmim, but the experimental results change by less than a factor of 2. The trend can be rationalized as follows: the carbon dioxide only experiences the local friction of the pocket in which it is located. Even though the presence of more viscous regions can slow the randomization of the total liquid structure and will restrict the motions of the less viscous regions, they do not completely determine the friction felt locally by CO_2. This behavior has been documented before with translational diffusion for neutral solutes in ILs[75,76] and aqueous solutions:[77] as the solute becomes either the same size as or smaller than the solvent molecules, the ratio of the friction measured to that predicted with slip boundary conditions becomes less than 1.

The results show that the chain length influences the reorientation dynamics in the ionic regions even if it does not directly mirror the bulk viscosity changes. For CO_2 to undergo complete orientational relaxation, the bulk ions have to undergo structural reconfiguration to move out of the way. The time dependence of ionic region restructuring slows as the

DOI: 10.1021/acs.jpcb.6b03971
J. Phys. Chem. B 2016, 120, 6698−6711

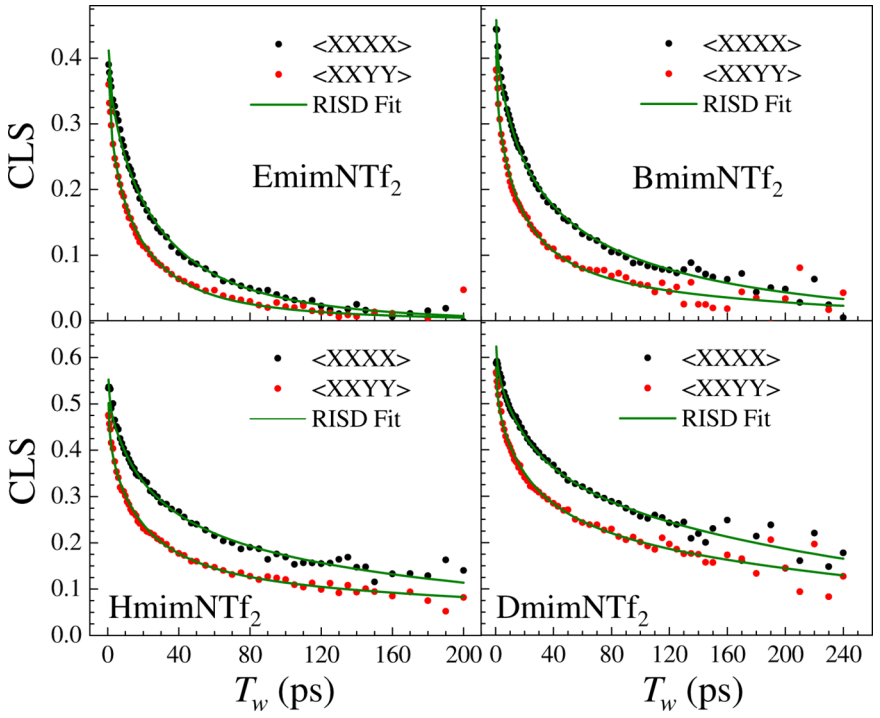

Figure 6. Plots of spectral diffusion as quantified by the CLS method in the ⟨*XXXX*⟩ (black) and ⟨*XXYY*⟩ (red) polarization configurations for all four RTIL/CO_2 systems. The fact that ⟨*XXXX*⟩ differs from ⟨*XXYY*⟩ confirms the presence of RISD in these systems. The simultaneous fits to both polarizations, using the second-order Stark effect RISD theory with the measured anisotropy to fix the orientational contribution, are shown in green. The fits reproduce the data.

chain length increases due to the slowed dynamics of the nonpolar regions but not to the extent that the bulk viscosity increases. Thus, the formation of nonpolar regions affects the polar regions, but the domains still have separate and distinct dynamics. The influence of chain length on the properties of the ionic regions is also manifested as a change in the CO_2 absorption peak position and linewidth, as shown in Figure 2 and Table 1.

III.D. Spectral Diffusion. Measurement of spectral diffusion provides a window into the structural fluctuations of the RTILs. Spectral diffusion reports on how long it takes for the probe molecules to completely sample the frequencies in the inhomogeneously broadened absorption line and thus how long it takes the system's structures to evolve so that all configurations that give rise to inhomogeneous broadening are experienced by the probe. As described briefly above, spectral diffusion is measured with 2D IR spectroscopy, in which three excitation pulses impinge on the sample and give rise to the vibrational echo pulse, which is self-heterodyned by the third excitation pulse that also serves as the LO.[45] The time between pulses 1 and 2 is the coherence time, τ; the time between pulses 2 and 3 is the population time, T_w. Data are collected by scanning τ with fixed T_w and obtaining a 2D spectrum. Then, T_w is changed and another 2D spectrum is obtained. The information on the structural evolution of the system is contained in the change in shape of the 2D spectra with T_w.

The amplitudes and time scales of spectral diffusion are quantified by the frequency-frequency correlation function (FFCF). The FFCF is the joint probability that a vibrational oscillator with an initial frequency will have that same frequency at a later time, averaged over all of the initial frequencies in the inhomogeneous spectral distribution. The center line slope (CLS) method[78,79] is used to extract the FFCF from the T_w dependence of the shape of the 2D IR spectra. The FFCF was modeled with the standard form

$$C(t) = \langle \delta\omega(t)\delta\omega(0)\rangle = \sum_i \Delta_i^2 \exp(-t/\tau_i) \tag{7}$$

where Δ_i and τ_i are the frequency fluctuation amplitude and time constant, respectively, of the ith component. A component of the FFCF is motionally narrowed and a source of homogeneous broadening in the absorption line if $\tau\Delta < 1$. In this instance, it is not possible to determine Δ and τ separately. The motionally narrowed contribution to the absorption spectrum has a pure dephasing linewidth, given by $\Gamma^* = \Delta^2\tau/\pi = 1/(\pi T_2^*)$, where T_2^* is the pure dephasing time. The total homogeneous dephasing time that is measured, T_2, also depends on the transition dipole orientational relaxation and vibrational lifetime and is given by

$$\frac{1}{T_2} = \frac{1}{T_2^*} + \frac{1}{2T_1} + \frac{1}{3T_{or}} \tag{8}$$

where T_1 and T_{or} are the vibrational lifetime and orientational relaxation time, respectively. CLS has been previously shown to be mathematically equivalent to the normalized T_w-dependent portion of the FFCF.[78,79]

If the probe sampled only the solvent's structural fluctuations, this would be the complete picture. However, it has recently been shown[40,41] that the probe itself may rotate on a time scale fast enough that the surrounding fluid serves as a source of a semistatic electric field. The rotation of the probe causes a change in its interaction with the electric field via the Stark effect (second order for CO_2). Therefore, the probe's vibrational frequency will change via the time-dependent Stark effect, which is in addition to the change in frequency caused by the structural evolution of the RTIL.[39] This RISD would then

DOI: 10.1021/acs.jpcb.6b03971
J. Phys. Chem. B 2016, 120, 6698−6711

need to be accounted for in fitting overall spectral diffusion. Otherwise, the presence of RISD causes the measured spectral diffusion to look as though it is proceeding faster than the contribution from the SSD alone. Note that if all of the spectral diffusion occurs faster than all components of the orientational relaxation, no effect will be observed.

To determine whether RISD is occurring, two polarization configuration 2D IR experiments were performed, that is, $\langle XXXX \rangle$ (parallel) and $\langle XXYY \rangle$ (perpendicular), where an X indicates a beam polarized horizontally and Y is polarized vertically. In the $\langle XXYY \rangle$ configuration, the first two pulses are vertical, whereas the third pulse and echo are horizontal. If the decays differ in their time dependence, then RISD is present and must be accounted for in the data analysis. Because RISD has been observed with vibrational probes in ILs[40,41,80] and, in particular, was present in the CO_2/EmimNTf$_2$ system,[39] it was anticipated that it would occur in the longer chain RTILs studied here. RISD does not always occur, as has been shown for bulk water.[40] Figure 6 displays the CLS decay data for the four RTILs in the parallel and perpendicular polarization configurations. The difference between the parallel and perpendicular decays for the four liquids shows that RISD must be taken into account to analyze the data and separate the time dependence of the SSD from that of RISD.

Whereas the individual parallel and perpendicular 2D spectra yield CLS decays, the FFCFs derived from them have contributions from the structural evolution of the liquids and the RISD. An MD simulation would contain both SSD and RISD, but it would not correspond to either the parallel or perpendicular data because simulations do not generally include the radiation fields that give rise to the anisotropic distribution of initially excited molecules. However, the parallel and perpendicular 2D spectra at each T_w can be combined to yield the isotropic data.[39] Then, spectral diffusion can be extracted from these isotropic spectra, using the CLS method. The isotropic CLS decay and corresponding isotropic FFCF provide the time dependence, including both structural fluctuations and reorientation-induced frequency fluctuations, but with molecules weighted equally, independent of the light polarization. Plots of the isotropic CLS decays are shown in Figure 7. These curves correspond to what could be extracted from an MD simulation. The FFCF parameters for the isotropic spectral diffusion decays for the RTILs with different chain lengths are available in Table S1.

Accounting for RISD in the CLS of 2D IR spectra taken in the $\langle XXXX \rangle$ and $\langle XXYY \rangle$ configurations to obtain the SSD involves separating this polarization-weighted (normalized) FFCF into the RISD correlation function, $R_p^{(2)}(t)$, and structural correlation function of the surrounding medium. Whereas the former is determined by the rotational dynamics of the probe and choice of polarizations used to interrogate the system, the latter is the information we are primarily interested in, as it directly reports on the structural changes in the RTIL that influence the probe molecule. Dynamic changes in structure lead to changing electric fields, which are experienced by the carbon dioxide molecules. For a probe molecule with a permanent dipole moment, RISD theory involves the first-order Stark effect.[41] However, CO_2 does not have a permanent dipole moment, and the second-order Stark effect RISD theory is employed.[39] It is important to note that the theory was derived with the assumption that the environment is not altered by the rotation of the probe. This is reasonable for CO_2 surrounded by large ions.

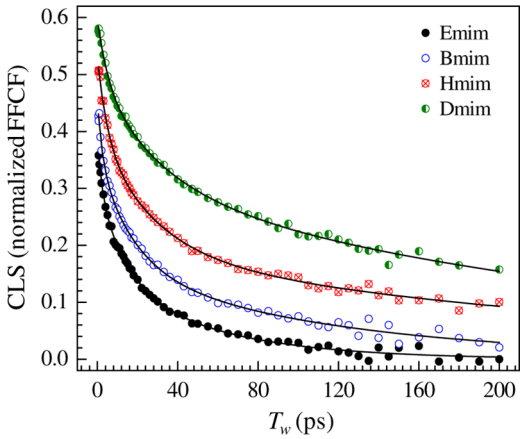

Figure 7. Isotropic spectral diffusion of carbon dioxide's asymmetric stretch in the RTILs, as quantified by the CLS method. Isotropic 2D IR spectra from which the CLS decays were obtained were constructed from the measured polarization configuration data as $\langle XXXX \rangle + 2\langle XXYY \rangle$. Solid black lines are triexponential fits to the decay curves; the resulting complete FFCF parameters are available in Table S1. The isotropic curves have contributions from SSD and RISD but do not contain polarization weighting. These are the curves that can be compared to those of MD simulations.

The second-order Stark effect RISD theory permits the separation of the scalar magnitude and direction of the electric-field fluctuations. The polarization-weighted FFCF within the second-order Stark model is given by

$$C_p(t) = \langle \delta\omega(t)\delta\omega(0) \rangle_p = F_s(t) + F_v(t)R_p^{(2)}(t) \tag{9}$$

where $F_s(t)$ is the correlation function of the scalar-coupled frequency fluctuations and $F_v(t)$ is the correlation function of frequency fluctuations with vectorial coupling to the electric field. The scalar correlation function depends on the squares of the field magnitudes alone at two time points. On the other hand, the vector correlation function depends on not only the squared magnitudes but also the electric field orientations at two time points. These could have different decay rates and/or functional forms, depending on the correlation between field magnitude and direction fluctuations.[39] In addition, the scalar term can contain any coupling between the probe and medium that is not vectorial in nature, for example, isotropic density fluctuations.

$R_p^{(2)}(t)$ is the RISD correlation function for second-order Stark coupling, which depends on the polarization configuration p and is given by[39]

$$\begin{cases} R_{\langle XXXX \rangle}^{(2)}(t) = \dfrac{1}{175}\left[\dfrac{28 + 215C_2(t) + 72C_4(t)}{1 + 4/5C_2(t)}\right] \\ R_{\langle XXYY \rangle}^{(2)}(t) = \dfrac{1}{175}\left[\dfrac{-14 + 155C_2(t) - 36C_4(t)}{1 - 2/5C_2(t)}\right] \\ R_{\text{isotropic}}^{(2)}(t) = C_2(t) \end{cases} \tag{10}$$

Note that $C_2(t)$ is the second-order Legendre orientational correlation function that is measured in the anisotropy experiments discussed above (see Figure 4). $C_4(t)$ is the fourth-order Legendre correlation function that is obtained from $C_2(t)$ using the orientational diffusion model. The relationships between wobbling-in-a-cone correlation functions of different orders have been presented previously.[41] $R_p^{(2)}(t)$ is

DOI: 10.1021/acs.jpcb.6b03971
J. Phys. Chem. B 2016, 120, 6698−6711

Table 5. SSD Parameters from Fits to the CLS Data, Using the Second-Order Stark Effect Model for RISD

	F_s, scalar correlation				F_v, vector correlation		OKE[a]
IL	A_1	τ_1 (ps)	A_2	τ_2 (ps)	A_3	τ_3 (ps)	τ_{total} (ps)
$EmimNTf_2$	0.09 ± 0.02	20 ± 5	0.07 ± 0.02	77 ± 20	0.36 ± 0.01	57 ± 5	380 ± 10
$BmimNTf_2$	0.11 ± 0.01	18 ± 2	0.10 ± 0.01	175 ± 20	0.40 ± 0.01	106 ± 7	1090 ± 10
$HmimNTf_2$	0.13 ± 0.01	21 ± 2	0.15 ± 0.01	390 ± 50	0.43 ± 0.01	166 ± 13	1940 ±10
$DmimNTf_2$	0.14 ± 0.02	25 ± 4	0.26 ± 0.03	380 ± 60	0.36 ± 0.02	280 ± 50	4820 ± 80

[a]Complete randomization time of the neat IL, as determined from optical heterodyne-detected optical Kerr effect (OHD-OKE) measurements (from reference 82).

then completely determined from the anisotropy experiments, and the only free variables are those associated with SSD, both the scalar and vector correlation functions' contributions.

⟨*XXXX*⟩ and ⟨*XXYY*⟩ CLS curves for each chain length are fit simultaneously with the second-order Stark model. It was found that the scalar correlation function is described by a biexponential and the vector part by a single exponential. If two single exponentials are used, then the model does not fit to the data. If more exponentials are added, then they do not improve the fit; typically, the additional exponential terms settle to the same time constants or have zero amplitude. Additionally, fits with any other number of exponentials fail the Akaike information criterion test, which settles on the single-exponential vector, biexponential scalar correlation functions as the most probable model. The polarization-selective CLS decays for ⟨*XXXX*⟩ and ⟨*XXYY*⟩ data (black and red circles) and their simultaneous fits within the second-order Stark RISD model (green curves) are shown in Figure 6. Tabulated values from the fits are given in Table 5. In the fits, there are no adjustable parameters in the RISD portion of the correlation functions. Both the parallel and perpendicular curves for a given sample need to be reproduced using a single choice of the SSD correlation function parameters. As can be seen in Figure 6, the fits are very good.

Let us first consider the vector correlation function of the spectral diffusion. This is modeled with a single exponential. Regardless of the chain length, this contributes ∼0.4 in amplitude toward the overall normalized correlation function. As the chain length is increased, the time constant for this correlation decay slows. This behavior is in the same direction as the change in viscosity but does not scale in the same manner. As the chain length increases, the vector correlation function time increases, more than the increase in viscosity. The vector correlation function time increases by a factor of ∼5 when going from Emim to Dmim, whereas the viscosity only increases by a factor of ∼3.5. Thus, in the polar pockets the carbon dioxide is somewhat shielded from the fluctuations and overall dynamics of the IL as a whole but nonetheless feels them to some extent.

The scalar correlation function provides additional information. Note that across all IL chain lengths, the fast time constant is the same within experimental error, ∼20 ps. This suggests that it is tracking motions around the carbon dioxide that are unaffected by the extent of nonpolar aggregation. This component can also contain a scalar contribution to the frequency fluctuations that is not due to the Stark effect, such as density fluctuations that are relatively unchanged in the ionic regions for all alkyl chain lengths. This motion is completely unaffected by the presence or absence of nonpolar regions.

The second scalar fluctuation time constant shows completely different behavior and increases with chain length but levels off from n = 6 to 10, although the error bars are relatively large. This leveling-off occurs at the onset of large aggregations of nonpolar tails, which has been seen in simulations[25] and corresponds to the appearance of a clearly recognizable prepeak in the low-Q region of small-angle X-ray scattering structure functions.[24] The dynamic processes that contribute to these magnitude fluctuations of a longer time scale then directly report on the extent of nonpolar tail aggregation, which is felt even in the polar regions.

Finally, a comparison can be made among the CO_2 reorientation times, SSD times, and time for total randomization that is experimentally determined using OHD-OKE measurements.[81,82] The time constant for complete orientational randomization of the constituent ions in $EmimNTf_2$ is 380 ps, and the results for ILs with a longer chain length are even slower. Values are given in the last column of Table 5. The complete bulk liquid orientational relaxation times, which are the times for the liquid structures of the RTILs to completely randomize, are much longer than any component of the SSD or any component of the CO_2 orientational relaxation times. This comparison shows that it is not necessary to entirely randomize the bulk liquid structure to have complete spectral diffusion, that is, to completely sample all structures that give rise to the frequencies in the inhomogeneously broadened absorption line. Thus, the IL structures relevant in determining the solvation environment of a particular CO_2 molecule do not depend on the global structure of the the bulk liquid. This is in line with the carbon dioxide locating only in the polar region. Complete randomization of the components of the liquid structure that influence the CO_2 occurs even though the total liquid, including the nonpolar regions, have yet to randomize.

The CO_2−RTIL local interactions randomize because of relatively fast fluctuations within the polar region. These fluctuation rates are sensitive to the increasing partitioning of the medium into polar and apolar domains with increasing chain length because the structure of the polar regions and structural fluctuations are influenced by the chain length. Thus, tuning the alkyl chain length in 1-alkyl-3-methylimidazolium bis(trifluoromethylsulfonyl)imide ILs is a readily accessible way to gradually vary the structure and dynamics of the solvation environment of CO_2 without drastically changing the identity of that environment.

IV. CONCLUDING REMARKS

The opportunities for using ILs for carbon capture and other technological processes are advancing. Their low vapor pressure, stability, and tunable properties make RTILs attractive systems. However, given the number of alternatives, rational design born from careful characterization is useful. Here, we have described the dynamics of carbon dioxide in $EmimNTf_2$, a promising solvent for carbon capture, and three analogous RTILs with longer chain lengths. The carbon dioxide probe also allows us to examine the dynamics of the RTILs in light of

DOI: 10.1021/acs.jpcb.6b03971
J. Phys. Chem. B 2016, 120, 6698−6711

nanostructuring. Although the carbon dioxide is located in the polar regions of the ILs, the linear spectra show that the alkyl chain has an impact on the intermolecular interactions experienced by CO_2.

The carbon dioxide wobbling-in-a-cone orientational relaxation times and cone angles (see Tables 3 and 4) are remarkably similar and independent of alkyl chain length. The wobbling times and cone angles are determined by relatively short-time-scale constraints imposed on the CO_2 angular motions by the surrounding ions. The first cone angular sampling occurs within a set of ion configuration constraints that limit the extent of angular sampling. The second larger cone of angles can only be sampled when the constraints of the first cone relax. Then, a second set of constraint limits the angular sampling until these constraints relax and permits the final complete orientational randomization of the CO_2. (It is worth noting that there is a subtle difference between Emim and the other ILs in the wavelength dependence of the cone angle for the second cone and also in the size of the inertial cone, see Figure 5.) The fact that the cone decay times and cone angles are, on average, independent of chain length demonstrates that the ionic structures and short-time ionic dynamics that surround the carbon dioxide and give rise to the angular constraints are the same for the four RTILs within experimental error.

The time for total reorientation lengthens as the alkyl chain grows. Whereas part of this effect might be explained by the increase in viscosity with chain length, the rotational dynamics do not scale correspondingly and occur increasingly faster than the hydrodynamics viscosity-based prediction. The weaker dependence of complete reorientation time τ_m (second to last column of Table 3) on viscosity than that of calculated hydrodynamic reorientation times, which scale with the viscosity (last column in Table 3), suggests that the effective viscosity in the ionic regions does not grow with chain length in the same manner as that for measured bulk viscosity. The similarities in the wobbling times and cone angles show that, on short time scales, the dynamics are not influenced by alkyl chain length. However, chain length plays a significant role at a longer time scale of complete orientational relaxation, although not as pronounced as the chain length dependence of bulk viscosity.

The isotropic 2D IR data (Figure 7 and Table S1), which reflect both SSD and RISD dynamics, show that spectral diffusion slows as the chain length increases. This is, perhaps, not surprising given the increase in viscosity. The difference in the time dependence of the data for different polarization configurations requires analysis using the RISD method, which permits the SSD to be separated from the RISD, and yields the SSD correlation functions for the vector and scalar fluctuations of the electric field. These show that the vector fluctuations slow in correlation decay considerably as the chain length increases and, in fact, slow more than the increase in viscosity. The fastest component of the spectral diffusion, which is scalar in nature, shows no chain-length dependence within experimental error. Thus, like the short-time-scale wobbling motions, the short-time-scale dynamics that gives rise to spectral diffusion does not depend on alkyl chain length. The slow scalar fluctuations become slower with chain length but reach a maximum relaxation time at the onset of large-scale nonpolar aggregation, around $n = 6$. This result suggests that once there are substantial nonpolar regions, making these regions larger does not change the longer-time-scale spectral diffusion dynamics experienced by CO_2 in the ionic regions.

For the most part, the fast motions of the carbon dioxide are conserved as the alkyl chain is lengthened and the slow motions slow. All of the orientational dynamics and spectral diffusion dynamics are fast compared to the time required for the bulk liquid to completely randomize its structure. Thus, the RTIL structural dynamics which influence CO_2, enabling it to randomize its orientation and frequency, do not depend on randomization of the global RTIL structure.

If a process is to be optimized in carbon capture (e.g., a reaction to convert the trapped carbon dioxide to another useful form), then the dynamics that actually influences CO_2 should be considered. The bulk viscosity may be a poor indicator of structural dynamics experienced by CO_2 or other solutes that locate in specific regions of RTILs. Future work could provide additional insights by examining the temperature dependence of the dynamics. Studying other types of cations and anions will provide more information, and if RTILs are to be used for carbon capture, then the effect of water, which is easily picked up by generally hygroscopic ILs, should also be investigated.

■ ASSOCIATED CONTENT

Supporting Information

The Supporting Information is available free of charge on the ACS Publications website at DOI: 10.1021/acs.jpcb.6b03971.

Includes plots of the population relaxation and kinetic model fits and the FFCF parameters for the isotropic data shown in Figure 7 (PDF)

■ AUTHOR INFORMATION

Corresponding Author

*E-mail: fayer@stanford.edu. Phone: (650) 723-4446.

Notes

The authors declare no competing financial interest.

■ ACKNOWLEDGMENTS

This work was funded by the Division of Chemical Sciences, Geosciences, and Biosciences, Office of Basic Energy Sciences of the U.S. Department of Energy through Grant # DE-FG03-84ER13251 (experiments using the shorter pulse ultrafast IR spectrometer). This material is also based on work supported by the Division of Chemistry, Directorate of Mathematical and Physical Sciences, National Science Foundation (NSF) (CHE-1461477) (experiments using the pulse-shaping ultrafast IR spectrometer and OHD-OKE spectrometer). M.D.F. would like to thank the Stanford Center for Carbon Storage research consortium in the School of Earth, Energy, and Environmental Sciences at Stanford University for partial support of this research.

■ REFERENCES

(1) Gasser, T.; Guivarch, C.; Tachiiri, K.; Jones, C. D.; Ciais, P. Negative Emissions Physically Needed to Keep Global Warming Below 2°C. *Nat. Commun.* **2015**, *6*, No. 7958, DOI: 10.1038/ncomms8958.

(2) Haszeldine, R. S. Carbon Capture and Storage: How Green Can Black Be? *Science* **2009**, *325*, 1647−1652.

(3) Lu, A. H.; Dai, S. *Porous Materials for Carbon Dioxide Capture*; Springer: Berlin, Heidelberg, 2014.

(4) Boot-Handford, M. E.; Abanades, J. C.; Anthony, E. J.; Blunt, M. J.; Brandani, S.; Mac Dowell, N.; Fernandez, J. R.; Ferrari, M.-C.; Gross, R.; Hallett, J. P.; et al. Carbon Capture and Storage Update. *Energy Environ. Sci.* **2014**, *7*, 130−189.

(5) Eide, L. I.; Bailey, D. W. Capture Précombustion. *Oil & Gas Sci. Technol. - Rev. Inst. Fr. Pet.* **2005**, *60*, 475−484.
(6) Bailey, D. W.; Feron, P. H. M. Capture Post-Combustion. *Oil & Gas Sci. Technol. - Rev. Inst. Fr. Pet.* **2005**, *60*, 461−474.
(7) Figueroa, J. D.; Fout, T.; Plasynski, S.; McIlvried, H.; Srivastava, R. D. Advances in CO_2 Capture Technology—The U.S. Department of Energy's Carbon Sequestration Program. *Int. J. Greenhouse Gas Control* **2008**, *2*, 9−20.
(8) Merkel, T. C.; Lin, H.; Wei, X.; Baker, R. Power Plant Post-Combustion Carbon Dioxide Capture: An Opportunity for Membranes. *J. Membr. Sci.* **2010**, *359*, 126−139.
(9) Hayes, R.; Warr, G. G.; Atkin, R. Structure and Nanostructure in Ionic Liquids. *Chem. Rev.* **2015**, *115*, 6357−6426.
(10) Plechkova, N. V.; Seddon, K. R. Applications of Ionic Liquids in the Chemical Industry. *Chem. Soc. Rev.* **2008**, *37*, 123−150.
(11) Hallett, J. P.; Welton, T. Room-Temperature Ionic Liquids: Solvents for Synthesis and Catalysis. 2. *Chem. Rev.* **2011**, *111*, 3508−3576.
(12) Welton, T. Room-Temperature Ionic Liquids. Solvents for Synthesis and Catalysis. *Chem. Rev.* **1999**, *99*, 2071−2084.
(13) Torralba-Calleja, E.; Skinner, J.; Gutierrez-Tauste, D. CO_2 Capture in Ionic Liquids: A Review of Solubilities and Experimental Methods. *J. Chem.* **2013**, *2013*, 473584.
(14) Condemarin, R.; Scovazzo, P. Gas Permeabilities, Solubilities, Diffusivities, and Diffusivity Correlations for Ammonium-Based Room Temperature Ionic Liquids with Comparison to Imidazolium and Phosphonium RTIL Data. *Chem. Eng. J.* **2009**, *147*, 51−57.
(15) Shannon, M. S.; Bara, J. E. Properties of Alkylimidazoles as Solvents for CO_2 Capture and Comparisons to Imidazolium-Based Ionic Liquids. *Ind. Eng. Chem. Res.* **2011**, *50*, 8665−8677.
(16) Bates, E. D.; Mayton, R. D.; Ntai, I.; Davis, J. H. CO_2 Capture by a Task-Specific Ionic Liquid. *J. Am. Chem. Soc.* **2002**, *124*, 926−927.
(17) Bara, J. E.; Camper, D. E.; Gin, D. L.; Noble, R. D. Room-Temperature Ionic Liquids and Composite Materials: Platform Technologies for CO_2 Capture. *Acc. Chem. Res.* **2010**, *43*, 152−159.
(18) Zhang, X.; Zhang, X.; Dong, H.; Zhao, Z.; Zhang, S.; Huang, Y. Carbon Capture with Ionic Liquids: Overview and Progress. *Energy Environ. Sci.* **2012**, *5*, 6668−6681.
(19) Ramdin, M.; de Loos, T. W.; Vlugt, T. J. H. State-of-the-Art of CO_2 Capture with Ionic Liquids. *Ind. Eng. Chem. Res.* **2012**, *51*, 8149−8177.
(20) Rocha, M. A. A.; Bastos, M.; Coutinho, J. A. P.; Santos, L. M. N. B. F. Heat Capacities at 298.15 K of the Extended $[C_nC_1IM][NTf_2]$ Ionic Liquid Series. *J. Chem. Thermodyn.* **2012**, *53*, 140−143.
(21) Rocha, M. A. A.; Lima, C. F. R. A. C.; Gomes, L. R.; Schröder, B.; Coutinho, J. A. P.; Marrucho, I. M.; Esperança, J. M. S. S.; Rebelo, L. P. N.; Shimizu, K.; Lopes, J. N. C.; et al. High-Accuracy Vapor Pressure Data of the Extended $[C_nC_1IM][NTf_2]$ Ionic Liquid Series: Trend Changes and Structural Shifts. *J. Phys. Chem. B* **2011**, *115*, 10919−10926.
(22) Rocha, M. A. A.; Neves, C. M. S. S.; Freire, M. G.; Russina, O.; Triolo, A.; Coutinho, J. A. P.; Santos, L. M. N. B. F. Alkylimidazolium Based Ionic Liquids: Impact of Cation Symmetry on Their Nanoscale Structural Organization. *J. Phys. Chem. B* **2013**, *117*, 10889−10897.
(23) Fruchey, K.; Fayer, M. D. Dynamics in Organic Liquids in Distinct Regions Using Charged and Uncharged Orientational Relaxation Probes. *J. Phys. Chem. B* **2010**, *114*, 2840−2845.
(24) Russina, O.; Triolo, A.; Gontrani, L.; Caminiti, R.; Xiao, D.; Hines, L. G., Jr.; Bartsch, R. A.; Quitevis, E. L.; Pleckhova, N.; Seddon, K. R. Morphology and Intermolecular Dynamics of 1-Alkyl-3-Methylimidazolium Bis{(Trifluoromethane)Sulfonyl}Amide Ionic Liquids: Structural and Dynamic Evidence of Nanoscale Segregation. *J. Phys.: Condens. Matter* **2009**, *21*, 424121.
(25) Shimizu, K.; Bernardes, C. E. S.; Canongia Lopes, J. N. Structure and Aggregation in the 1-Alkyl-3-Methylimidazolium Bis-(Trifluoromethylsulfonyl)Imide Ionic Liquid Homologous Series. *J. Phys. Chem. B* **2014**, *118*, 567−576.
(26) Cadena, C.; Anthony, J. L.; Shah, J. K.; Morrow, T. I.; Brennecke, J. F.; Maginn, E. J. Why is CO_2 so Soluble in Imidazolium-Based Ionic Liquids? *J. Am. Chem. Soc.* **2004**, *126*, 5300−5308.
(27) Armand, M.; Endres, F.; MacFarlane, D. R.; Ohno, H.; Scrosati, B. Ionic-Liquid Materials for the Electrochemical Challenges of the Future. *Nat. Mater.* **2009**, *8*, 621−629.
(28) Shirota, H.; Mandai, T.; Fukazawa, H.; Kato, T. Comparison Between Dicationic and Monocationic Ionic Liquids: Liquid Density, Thermal Properties, Surface Tension, and Shear Viscosity. *J. Chem. Eng. Data* **2011**, *56*, 2453−2459.
(29) Yokozeki, A.; Shiflett, M. B.; Junk, C. P.; Grieco, L. M.; Foo, T. Physical and Chemical Absorptions of Carbon Dioxide in Room-Temperature Ionic Liquids. *J. Phys. Chem. B* **2008**, *112*, 16654−16663.
(30) Moganty, S. S.; Baltus, R. E. Diffusivity of Carbon Dioxide in Room-Temperature Ionic Liquids. *Ind. Eng. Chem. Res.* **2010**, *49*, 9370−9376.
(31) Umecky, T.; Kanakubo, M.; Makino, T.; Aizawa, T.; Suzuki, A. Effect of CO_2 Dissolution on Electrical Conductivity and Self-Diffusion Coefficients of 1-Butyl-3-Methylimidazolium Hexafluorophosphate Ionic Liquid. *Fluid Phase Equilib.* **2013**, *357*, 76−79.
(32) Hou, Y.; Baltus, R. E. Experimental Measurement of the Solubility and Diffusivity of CO_2 in Room-Temperature Ionic Liquids Using a Transient Thin-Liquid-Film Method. *Ind. Eng. Chem. Res.* **2007**, *46*, 8166−8175.
(33) Camper, D.; Becker, C.; Koval, C.; Noble, R. Diffusion and Solubility Measurements in Room Temperature Ionic Liquids. *Ind. Eng. Chem. Res.* **2006**, *45*, 445−450.
(34) Kortenbruck, K.; Pohrer, B.; Schluecker, E.; Friedel, F.; Ivanovic-Burmazovic, I. Determination of the Diffusion Coefficient of CO_2 in the Ionic Liquid Emim NTf2 Using Online FTIR Measurements. *J. Chem. Thermodyn.* **2012**, *47*, 76−80.
(35) Morgan, D.; Ferguson, L.; Scovazzo, P. Diffusivities of Gases in Room-Temperature Ionic Liquids: Data and Correlations Obtained Using a Lag-Time Technique. *Ind. Eng. Chem. Res.* **2005**, *44*, 4815−4823.
(36) Moya, C.; Palomar, J.; Gonzalez-Miquel, M.; Bedia, J.; Rodriguez, F. Diffusion Coefficients of CO_2 in Ionic Liquids Estimated by Gravimetry. *Ind. Eng. Chem. Res.* **2014**, *53*, 13782−13789.
(37) Hazelbaker, E. D.; Budhathoki, S.; Katihar, A.; Shah, J. K.; Maginn, E. J.; Vasenkov, S. Combined Application of High-Field Diffusion NMR and Molecular Dynamics Simulations to Study Dynamics in a Mixture of Carbon Dioxide and an Imidazolium-Based Ionic Liquid. *J. Phys. Chem. B* **2012**, *116*, 9141−9151.
(38) Brinzer, T.; Berquist, E. J.; Ren, Z.; Dutta, S.; Johnson, C. A.; Krisher, C. S.; Lambrecht, D. S.; Garrett-Roe, S. Ultrafast Vibrational Spectroscopy (2D-IR) of CO_2 in Ionic Liquids: Carbon Capture from Carbon Dioxide's Point of View. *J. Chem. Phys.* **2015**, *142*, 212425.
(39) Giammanco, C. H.; Kramer, P. L.; Yamada, S. A.; Nishida, J.; Tamimi, A.; Fayer, M. D. Carbon Dioxide in an Ionic Liquid: Structural and Rotational Dynamics. *J. Chem. Phys.* **2016**, *144*, 104506.
(40) Kramer, P. L.; Nishida, J.; Giammanco, C. H.; Tamimi, A.; Fayer, M. D. Observation and Theory of Reorientation-Induced Spectral Diffusion in Polarization-Selective 2D IR Spectroscopy. *J. Chem. Phys.* **2015**, *142*, 184505.
(41) Kramer, P. L.; Nishida, J.; Fayer, M. D. Separation of Experimental 2D IR Frequency-Frequency Correlation Functions into Structural and Reorientation-Induced Contributions. *J. Chem. Phys.* **2015**, *143*, 124505.
(42) Maiella, P. G.; Schoppelrei, J. W.; Brill, T. B. Spectroscopy of Hydrothermal Reactions. Part XI: Infrared Absorptivity of CO_2 and N_2O in Water at Elevated Temperature and Pressure. *Appl. Spectrosc.* **1999**, *53*, 351−355.
(43) Moore, G.; Chizmeshya, A.; McMillan, P. F. Calibration of a Reflectance FTIR Method for Determination of Dissolved CO_2 Concentration in Rhyolitic Glasses. *Geochim. Cosmochim. Acta* **2000**, *64*, 3571−3579.
(44) Fenn, E. E.; Wong, D. B.; Fayer, M. D. Water Dynamics in Small Reverse Micelles in Two Solvents: Two-Dimensional Infrared

DOI: 10.1021/acs.jpcb.6b03971
J. Phys. Chem. B 2016, 120, 6698−6711

Vibrational Echoes with Two-Dimensional Background Subtraction. *J. Chem. Phys.* **2011**, *134*, 054512.
(45) Karthick Kumar, S. K.; Tamimi, A.; Fayer, M. D. Comparisons of 2D IR Measured Spectral Diffusion in Rotating Frames Using Pulse Shaping and in the Stationary Frame Using the Standard Method. *J. Chem. Phys.* **2012**, *137*, 184201.
(46) Park, S.; Kwak, K.; Fayer, M. D. Ultrafast 2D-IR Vibrational Echo Spectroscopy: A Probe of Molecular Dynamics. *Laser Phys. Lett.* **2007**, *4*, 704−718.
(47) Gallagher Faeder, S. M.; Jonas, D. M. Two-Dimensional Electronic Correlation and Relaxation Spectra: Theory and Model Calculations. *J. Phys. Chem. A* **1999**, *103*, 10489−10505.
(48) Shim, S.-H.; Strasfeld, D. B.; Fulmer, E. C.; Zanni, M. T. Femtosecond Pulse Shaping Directly in the Mid-IR Using Acousto-Optic Modulation. *Opt. Lett.* **2006**, *31*, 838−840.
(49) Shim, S.-H.; Zanni, M. T. How to Turn Your Pump-Probe Instrument into a Multidimensional Spectrometer: 2D IR and Vis Spectroscopies via Pulse Shaping. *Phys. Chem. Chem. Phys.* **2009**, *11*, 748−761.
(50) Garrett-Roe, S.; Hamm, P. Purely Absorptive Three-Dimensional Infrared Spectroscopy. *J. Chem. Phys.* **2009**, *130*, 164510.
(51) Seki, T.; Grunwaldt, J.-D.; Baiker, A. In Situ Attenuated Total Reflection Infrared Spectroscopy of Imidazolium-Based Room-Temperature Ionic Liquids Under "Supercritical" CO_2. *J. Phys. Chem. B* **2009**, *113*, 114−122.
(52) Potoff, J. J.; Siepmann, J. I. Vapor−Liquid Equilibria of Mixtures Containing Alkanes, Carbon Dioxide, and Nitrogen. *AlChE J.* **2001**, *47*, 1676−1682.
(53) Huang, X.; Margulis, C. J.; Li, Y.; Berne, B. J. Why is the Partial Molar Volume of CO_2 So Small When Dissolved in a Room Temperature Ionic Liquid? Structure and Dynamics of CO_2 Dissolved in $[Bmim^+][PF^{6-}]$. *J. Am. Chem. Soc.* **2005**, *127*, 17842−17851.
(54) Giammanco, C. H.; Kramer, P. L.; Yamada, S. A.; Nishida, J.; Tamimi, A.; Fayer, M. D. Coupling of Carbon Dioxide Stretch and Bend Vibrations Reveals Thermal Population Dynamics in an Ionic Liquid. *J. Phys. Chem. B* **2016**, *120*, 549−556.
(55) Kramer, P. L.; Giammanco, C. H.; Fayer, M. D. Dynamics of Water, Methanol, and Ethanol in a Room Temperature Ionic Liquid. *J. Chem. Phys.* **2015**, *142*, 212408.
(56) Wong, D. B.; Giammanco, C. H.; Fenn, E. E.; Fayer, M. D. Dynamics of Isolated Water Molecules in a Sea of Ions in a Room Temperature Ionic Liquid. *J. Phys. Chem. B* **2013**, *117*, 623−635.
(57) Cammarata, L.; Kazarian, S. G.; Salter, P. A.; Welton, T. Molecular States of Water in Room Temperature Ionic Liquids. *Phys. Chem. Chem. Phys.* **2001**, *3*, 5192−5200.
(58) Steinel, T.; Asbury, J. B.; Zheng, J. R.; Fayer, M. D. Watching Hydrogen Bonds Break: A Transient Absorption Study of Water. *J. Phys. Chem. A* **2004**, *108*, 10957−10964.
(59) Rezus, Y. L. A.; Bakker, H. J. On the Orientational Relaxation of HDO in Liquid Water. *J. Chem. Phys.* **2005**, *123*, 114502.
(60) Kenkre, V. M.; Tokmakoff, A.; Fayer, M. D. Theory of Vibrational Relaxation of Polyatomic Molecules in Liquids. *J. Chem. Phys.* **1994**, *101*, 10618.
(61) Lipari, G.; Szabo, A. Effect of Librational Motion on Fluorescence Depolarization and Nuclear Magnetic-Resonance Relaxation in Macromolecules and Membranes. *Biophys. J.* **1980**, *30*, 489−506.
(62) Lipari, G.; Szabo, A. Model-Free Approach to the Interpretation of Nuclear Magnetic-Resonance Relaxation in Macromolecules.1. Theory and Range of Validity. *J. Am. Chem. Soc.* **1982**, *104*, 4546−4559.
(63) Wang, C. C.; Pecora, R. Time-Correlation Functions for Restricted Rotational Diffusion. *J. Chem. Phys.* **1980**, *72*, 5333−5340.
(64) Kinosita, K.; Ikegami, A.; Kawato, S. On the Wobbling-in-Cone Analysis of Fluorescence Anisotropy Decay. *Biophys. J.* **1982**, *37*, 461−464.
(65) Tan, H.-S.; Piletic, I. R.; Fayer, M. D. Orientational Dynamics of Water Confined on a Nanometer Length Scale in Reverse Micelles. *J. Chem. Phys.* **2005**, *122*, 174501.
(66) Andrews, S. S.; Boxer, S. G. Vibrational Stark Effects of Nitriles I. Methods and Experimental Results. *J. Phys. Chem. A* **2000**, *104*, 11853−11863.
(67) Boxer, S. G. Stark Realities. *J. Phys. Chem. B* **2009**, *113*, 2972−2983.
(68) Bublitz, G. U.; Boxer, S. G. Stark Spectroscopy: Applications in Chemistry, Biology, and Materials Science. *Annu. Rev. Phys. Chem.* **1997**, *48*, 213−242.
(69) Andrews, S. S. The Measurement and Physics of Vibrational Stark Effects. Ph.D Thesis, Stanford University, 2001.
(70) Moog, R. S.; Ediger, M. D.; Boxer, S. G.; Fayer, M. D. Viscosity Dependence of the Rotational Reorientation of Rhodamine B in Mono- and Polyalcohol. Picosecond Transient Grating Experiments. *J. Phys. Chem.* **1982**, *86*, 4694−4700.
(71) Youngren, G. K.; Acrivos, A. Rotational Friction Coefficients for Ellipsoids and Chemical Molecules with the Slip Boundary Condition. *J. Chem. Phys.* **1975**, *63*, 3846−3849.
(72) Hu, C.-M.; Zwanzig, R. Rotational Friction Coefficients for Spheroids with the Slipping Boundary Condition. *J. Chem. Phys.* **1974**, *60*, 4354−4357.
(73) Sension, R. J.; Hochstrasser, R. M. Comment on: Rotational Friction Coefficients for Ellipsoids and Chemical Molecules with Slip Boundary Conditions. *J. Chem. Phys.* **1993**, *98*, 2490−2490.
(74) Pauling, L. *The Nature of the Chemical Bond and the Structure of Molecules and Crystals: An Introduction to Modern Structural Chemistry*; Cornell University Press: Ithaca, NY, 1960.
(75) Kaintz, A.; Baker, G.; Benesi, A.; Maroncelli, M. Solute Diffusion in Ionic Liquids, NMR Measurements and Comparisons to Conventional Solvents. *J. Phys. Chem. B* **2013**, *117*, 11697−11708.
(76) Araque, J. C.; Yadav, S. K.; Shadeck, M.; Maroncelli, M.; Margulis, C. J. How is Diffusion of Neutral and Charged Tracers Related to the Structure and Dynamics of a Room-Temperature Ionic Liquid? Large Deviations from Stokes−Einstein Behavior Explained. *J. Phys. Chem. B* **2015**, *119*, 7015−7029.
(77) Edward, J. T. Molecular Volumes and the Stokes−Einstein Equation. *J. Chem. Educ.* **1970**, *47*, 261.
(78) Kwak, K.; Park, S.; Finkelstein, I. J.; Fayer, M. D. Frequency-Frequency Correlation Functions and Apodization in 2D-IR Vibrational Echo Spectroscopy: A New Approach. *J. Chem. Phys.* **2007**, *127*, 124503.
(79) Kwak, K.; Rosenfeld, D. E.; Fayer, M. D. Taking Apart the Two-Dimensional Infrared Vibrational Echo Spectra: More Information and Elimination of Distortions. *J. Chem. Phys.* **2008**, *128*, 204505.
(80) Tamimi, A.; Fayer, M. D. Ionic Liquid Dynamics Measured with 2D IR and IR Pump−Probe Experiments on a Linear Anion and the Influence of Potassium Cations. *J. Phys. Chem. B* **2016**, DOI: 10.1021/acs.jpcb.6b00409.
(81) Sturlaugson, A. L.; Arima, A. Y.; Bailey, H. E.; Fayer, M. D. Orientational Dynamics in a Lyotropic Room Temperature Ionic Liquid. *J. Phys. Chem. B* **2013**, *117*, 14775−14784.
(82) Tamimi, A.; Bailey, H.; Fayer, M. D. Alkyl Chain Length Dependence of the Dynamics and Structure in the Ionic Regions of Room Temperature Ionic Liquids. *J. Phys. Chem. B* **2016**, submitted.

DOI: 10.1021/acs.jpcb.6b03971
J. Phys. Chem. B 2016, 120, 6698−6711